J Mater Sci (2020) 55:2439–2453

Electronic materials

Highly stretchable, breathable and negative resistance variation textile strain sensor with excellent mechanical stability for wearable electronics

Kai Zhao[1], Wenbin Niu[1,*], and Shufen Zhang[1]

[1] State Key Laboratory of Fine Chemicals, Dalian University of Technology, West Campus, 2 Linggong Rd., Dalian 116024, People's Republic of China

Received: 20 August 2019
Accepted: 2 November 2019
Published online: 13 November 2019

ABSTRACT

In recent years, wearable and stretchable electronic devices have attracted great research interest and effort due to their promising applications in electronic skin, wearable health monitoring, human–machine interactions and so on. However, it still remains a great challenge to fabricate highly stretchable and wearable devices with excellent breathability, mechanical robustness and laundering durability. Herein, we fabricated a highly stretchable and breathable textile strain sensor based on conductive polyester fabric (CPF) with weft-knitted structure by chemically growing conductive and transparent Al-doped ZnO (AZO) element via atomic layer deposition (ALD). The CPF strain sensor demonstrates captivating performance, including high stretchability (up to 130%) and long-term stability (3000 cycles), as well as a distinct negative resistance variation with increasing strain owing to its weft-knitted structure. Most importantly, due to the formation of chemical interactions between textiles and AZO films during ALD process, the CPF strain sensor exhibits excellent mechanical robustness and laundering durability under reciprocating rubbing (50 kPa load pressure, 30 cycles), washing (500 r/min for 10 cycles, 200 min) and light fastness (accelerated light aging test for 7 days), thus allowing the fabrication of breathable and comfortable wearable sensor without elastomer encapsulation. Based on its admirable performances, the CPF strain sensor can be easily knitted or sewed on garments or attached on human skin directly for tracking both large and subtle human motions, revealing its numerous prospects in wearable electronics, intelligent robotics and other fields.

Address correspondence to E-mail: niuwb@dlut.edu.cn

https://doi.org/10.1007/s10853-019-04189-x

Introduction

In the past decade, researches on wearable and stretchable electronic devices have attained tremendous attention and have gained respectable progress [1–5]. Stretchable strain sensors, as a vital component of wearable electronic devices, can be comfortably worn and can convert physical deformations induced by human physiological activities and body movements into measurable signals [6–11]. Therefore, they have shown substantive potential applications in various areas, such as electronic skins [12–14], intelligent robotics [8, 15], personalized health monitoring [1, 16, 17] and smart human–machine interactions [18, 19]. Apart from some elastomer-based composite materials that can function as strain sensors [20–22], integrating various sensing components with stretchable substrates is an effective way for fabricating stretchable strain sensors [10, 16, 23]. The typically stretchable substrates usually involve polydimethylsiloxane (PDMS) [24–26], Ecoflex [16, 27], textile [28–31], rubbers and elastomeric polyurethanes [32–34]. Among them, textiles that are indispensable in our daily life have been extensively exploited as stretchable substrate for the prosperous development of wearable and flexible electronics due to their unique characteristics, including lightweight, flexibility, stretchability, breathability, washability, as well as their intrinsic warm and snug properties [35].

In order to impart the sensing functionality to textile, one promising and most commonly used approach is coating of conductive sensing elements directly on fabric [18, 28, 31, 36–40]. The obtained conductive fabric (CF) can maintain the above-mentioned unique and intrinsic characteristics of textile while displaying excellent electrical conductivity, thus ensuring its broad prospects in wearable electronics. Typically, textile strain sensors were obtained by integrating conductive sensing elements, such as metallic nanoparticles [37, 38], carbon nanotubes (CNTs) [28, 40] and graphene oxide (GO) [18, 28, 31, 36, 39] with textiles through interactions of hydrogen bonding, electrostatic and van der Waals forces. However, considering the weak interactions between textiles and sensing elements in using the coating methods, the lack of mechanical robustness and laundering durability is a big issue as the components can inevitably fall off after the sensor is frequently used or subjected to repeatedly mechanical rubbing and washing cycles, which greatly limits its practical applications. To address these issues, the vast majority of devices were encapsulated with elastic polymer matrix or incorporated with polymer nanocomposites [27, 30, 38, 41–45]. Unfortunately, these methods can result in many disadvantages, such as poor breathability, unsatisfying fit, low comfort with the human body and a complex preparation process. A desirable wearable textile strain sensor should possess the merits of highly stretchability, breathability, excellent mechanical robustness and laundering durability. Nevertheless, fabrication of the above-mentioned textile strain sensors remains challenging and is largely unexplored so far.

Recently, atomic layer deposition (ALD) has been investigated as an emerging and efficient method for the preparation of various types of thin film coatings due to its unique surface chemical adsorption and reaction characteristics, as well as superior conformability to the complex surfaces [46–49]. As a result, many functional materials can be readily deposited onto fiber or textile through ALD, thus endowing multifunctional capabilities for wearable electronics [50–54]. Al-doped ZnO (AZO), as one of the conductive elements that can be grown via ALD, provides a promising alternative for the fabrication of conductive sensing textile owing to its low cost, abundant resource, nontoxicity and good stability [55–58]. Therefore, we surmised that a novel textile strain sensor can be realized through growing conductive and transparent AZO film on the textile surface by ALD technique. The formation of chemical bonding between AZO films and textile during ALD process will enable textile strain sensor excellent mechanical robustness and laundering durability.

In this work, we propose a strategy based on ALD to develop a highly stretchable conductive polyester fabric (CPF) strain sensor, which can be fabricated by growing conductive and transparent AZO films on the weft-knitted polyester fabric. Notably, strong chemical interactions between textile and sensing element instead of weak forces enable the CPF strain sensor excellent mechanical robustness and laundering durability without further elastomer encapsulation, thus endowing the sensor with superior breathability and great comfort to the human body. In addition, the weft-knitted structure of CPF induces the sensor to exhibit a distinct negative resistance variation with increasing strain. It should be

mentioned that recent works have reported strain sensors with negative gauge factors, but the relatively small workable range will restrict their practical applications [31, 59]. The CPF strain sensor shows combined superiority of large workable range up to 130%, sensitivity (GF of − 2.12 under 0–20%, that of − 0.41 under 20–80% and that of − 0.06 under 80–130%) and long-term stability (3000 cycles), which can be easily knitted or sewed on garments directly for wearable applications. We further demonstrate versatile capabilities of the CPF strain sensor in detection of both large deformations (joint movement) and subtle movements (facial expressions, phonation, etc.) of the human body, revealing numerous potential applications in wearable electronic devices, healthcare monitors, intelligent robotics and so forth.

Experimental section

Materials

Trimethyl aluminum (TMA, 99.999%) and diethyl zinc (DEZ, 99.999%) were purchased from AiMouYuan Scientific Equipment Co., Ltd (Nanjing, China). Commercially available polyester fabrics were supplied by Changxing DAXIN Textile Co., Ltd. Deionized water and nitrogen (99.999%) were produced by Dalian University of Technology and Dalian GuangMing Special Gas Co., Ltd, respectively. Silver paste was provided by Jiangsu Shenggelu New Material Technology Co., Ltd.

Preparation of the CPF

The polyester fabrics with the weft-knitted structure were utilized as raw materials. Firstly, the fabrics were rinsed using deionized water for 30 min with ultrasonication to eliminate impurity. After being dried thoroughly in air, the polyester fabrics were then placed in a plasma cleaner using air as plasma source (15 Pa, 25 °C, 10.2 W, Shenyang Kejing Auto-Instrument Co., Ltd) for 10 min, in which many highly active hydrophilic groups can be introduced onto the surfaces, thus facilitating the following deposition process. Subsequently, AZO films were deposited onto the fabric surfaces at 150 °C by the ALD method. To verify that the substrate is not damaged under this circumstance, the polyester fabric was placed in reaction chamber at 150 °C in vacuum with inert gas N_2 for 6 h. Figure S1 shows the photographs and SEM images of polyester fabric before and after thermal treatment, demonstrating its intrinsic morphology and structure were not be affected at this temperature. In AZO deposition procedure, diethyl zinc [DEZ; $Zn(C_2H_5)_2$], trimethyl aluminum [TMA; $Al(CH_3)_3$] and deionized water (DI; H_2O) were used as the precursors for Zn, Al and O, respectively. High-purity nitrogen (N_2) was used as the carrier gas at a flow rate of 20 sccm (standard cubic centimeters per minute). During the deposition process, the treated polyester fabrics were put in the reaction chamber (LabNano™, Beijing Ensure Nanotech Co., Ltd), and then, the temperature was raised to 150 °C in vacuum. Next H_2O and DEZ were alternatively pulsed into the ALD reactor to deposit ZnO layer according to the following sequence: H_2O (0.02 s)/N_2 (20 s)/DEZ (0.02 s)/N_2 (20 s). These comprise a complete ZnO cycle. For Al doping into the ZnO films, a single Al_2O_3 cycle, conforming to the sequence: H_2O (0.02 s)/N_2 (20 s)/TMA (0.02 s)/N_2 (20 s), was inserted after 15 cycles of ZnO layers. Subsequently, 15 ZnO cycles and one Al_2O_3 cycle were repeatedly deposited for AZO films, and the total supercycle was set to 25. Hence, the AZO films, in which the ratio of ZnO:Al_2O_3 ALD cycles was fixed to 15 invariably, were deposited onto the fabric surfaces. Finally, the conductive polyester fabrics were cooled to room temperature and took out of the reaction chamber.

Preparation of the CPF strain sensor

The conductive polyester fabric was firstly cut into rectangular shape with the size of 2.5 × 1.0 cm. Then silver paste was applied to connect both sides of the polyester fabric with two copper strips, followed by curing at 80 °C for 2 h to obtain the textile strain sensor without any encapsulation.

Breathability measurements

To quantitatively demonstrate the breathability of the polyester fabric before and after AZO deposition, the water vapor transmittance (WVT) rate was tested according to the ASTM standard E96 water method. Briefly, the fabric was covered on the beaker containing 30 mL of water (Fig. S2). The mass of the tested beaker was recorded at a temperature of 20 °C

and a relative humidity of 61% for 5 h. The WVTR value was calculated based on the equation below.

$$\text{WVT rate} = \frac{m_1 - m_2}{5S}$$

where m_1 and m_2 are the mass of the beaker before and after measurements, respectively. S is the test area.

Characterization of the CPF strain sensor

The surface morphologies of the textile strain sensor and the cross-sectional images of the AZO films were characterized by a Nova NanoSEM 450 scanning electron microscope with an acceleration voltage of 25 kV. EDS mapping analysis was performed using a Nova NanoSEM 450 scanning electron microscope equipped with an inbuilt EDS detector. FT-IR spectra were recorded using a Thermo Fisher iN 10 spectrometer with KBr method. XPS (Thermo Scientific Escalab Xi^+) measurements were taken using Al Kα radiation source. Optical images of the CPF strain sensor morphology at different strains were obtained using an angle-resolved microspectroscopy system (ARM, Ideaoptics, PR China). Digital photographs were captured with a Nikon D7000 digital camera. Water contact angles were measured using a Dataphysics OCA 30 system (Germany) with a 3 μL droplet at room temperature. For the electromechanical properties of the textile strain sensor, the mechanical tensile measurements were taken by a universe testing machine (PT-305, Dongguan Precise Test Equipment Co., Ltd). The resistances were recorded by a Keysight 3440A/11A Digital Multimeter (Agilent) in conjunction with the computer-controlled universe testing machine through a two-wire model.

Mechanical stability measurements

Rubbing resistance measurement was taken on a YB571-II crockmeter (Wenzhou Darong Textile Standard Instrument Factory, China) according to the ISO 105 × 12 standard. Both ends of the CPF were first fixed to the cotton using cellotape, and the CPF was subjected to reciprocating rubbing for 30 times using a loaded head (with a pressure of 50 kPa). For the laundering durability measurement, the CPF was placed in a beaker containing 200 mL of water with magnetically stirring at 500 r/min for 10 cycles. In order to simulate the real laundry machine environment, 0.2 mL of commercial laundry detergent (Blue moon, China) was added in advance, and each washing cycle was set to 20 min. Light fastness was conducted using a YG(B)911-V type Sunlight Climate Tester (Wenzhou Darong Textile Standard Instrument Factory) according to the standard of ISO 105-B02 for 7 days. The temperature in the reactor chamber was set to 40 °C, and the humidity was 50% RH. A xenon arc lamp with irradiance of 1.1 W m^{-2} at 420 nm was used to irradiate the CPF sample.

Results and discussion

Fabrication process of the CPF strain sensor

Figure 1 presents the fabrication process of the CPF strain sensor through ALD method. Here, we choose the weft-knitted polyester fabrics with superior tensile performance as the inert substrates [31, 38, 60]. Before AZO deposition, the surfaces of pristine polyester fabric were activated by plasma treatment. In this process, a series of highly active hydrophilic oxygen-containing functional groups could be introduced onto the fabric surfaces in order to facilitate the initiation of ZnO growth via ALD (Figs. S4 and S5) [47, 61, 62], which is the prerequisite for the deposition of AZO films on the polyester fabric. During the deposition process, diethyl zinc [DEZ; $Zn(C_2H_5)_2$], served as the precursor for ZnO, was first introduced into the reactor; it reacted with those functional groups to form $–O–ZnC_2H_5$ owing to the surface chemical reactions [63, 64]. After purging by N_2, a second precursor deionized water (DI; H_2O) was pulsed to react with $–O–ZnC_2H_5$, in which a monolayer of ZnO with the outmost exposed –OH group was achieved through DEZ-DI cycle [62, 64]. The detailed reaction schemes for ZnO are presented in Scheme S1-2. This procedure would bring about the formation of chemical interactions between the AZO films and polyester surface, thus enhancing the adhesive capability remarkably (Fig. S4). After repeated depositing ZnO monolayer for 15 cycles, trimethyl aluminum [TMA; $Al(CH_3)_3$] and DI were alternatively pulsed into the reactor to realize Al doping in a similar way through TMA-DI cycle (Scheme S3-4). Finally, 15 cycles of DEZ-DI and doping TMA-DI cycle were repeated carried out for 25 times to finish the deposition of AZO films (Al doping level 4.76%), as shown in Fig. S6. The detailed

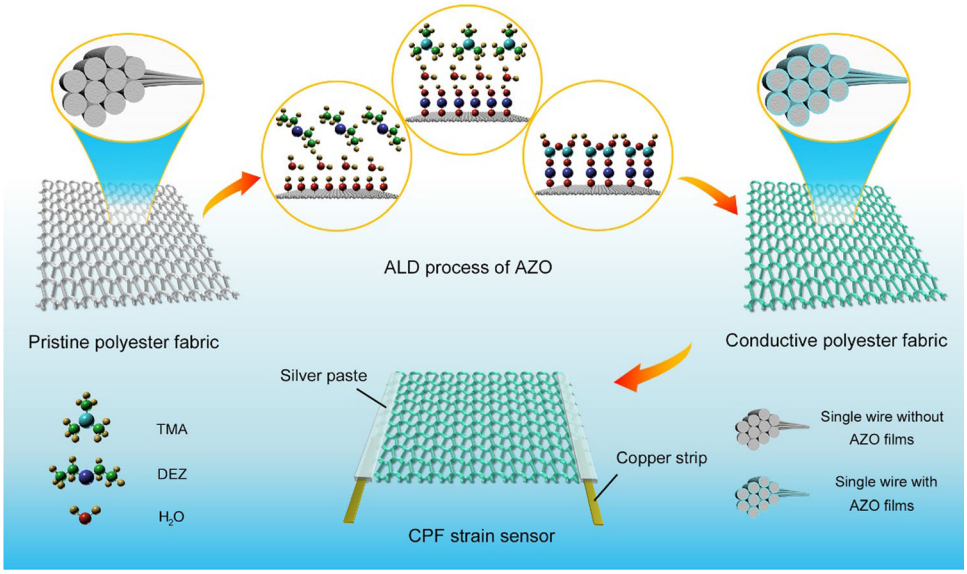

Figure 1 Schematic illustration of the CPF strain sensor fabrication process.

conducting mechanism of AZO films and selecting principle of deposition conditions are presented in Supporting Information. After finishing AZO deposition, silver paste was used to connect two copper strips on the two ends of the fabric as the electrodes, followed by curing at 80 °C for 2 h to obtain the CPF strain sensor without further encapsulation.

The morphologies and structures of the CPF strain sensor are shown in Fig. 2. Figure 2a presents the photograph of a pristine rectangular polyester fabric with the size of 2.5 × 1.0 cm. After depositing the conductive AZO films via ALD and connecting two copper strips with silver paste, the resulting strain sensor displayed a white color just the same as pristine fabric, which can be attributed to the excellent transparency of the AZO films (Fig. 2b). Figure 2c, d and S7 show typical scanning electron microscopy (SEM) images of the polyester fabric before and after AZO deposition with different magnifications. It can be seen that the weft-knitted structure and polyester fibers were well maintained after the AZO deposition, which guarantees its high stretchability of the CPF. Particularly, the porous structure of the polyester fabric, which is a crucial factor for its excellent breathability, was also retained very well, ensuring the intrinsically breathable characteristics of CPF as textiles (Fig. S7). In order to quantitatively compare the breathability of the polyester fabric before and after AZO deposition, the water vapor transmittance (WVT) rate was tested to assess the moisture permeability. As shown in Figure S3, the calculated WVT rates were 34.6 g/m^2 h and 33.2 g/m^2 h before and after AZO deposition, respectively, which are slightly less than the natural evaporation rate (52.5 g/m^2 h), indicating the excellent breathability of CPF. As expected, AZO films grown on single polyester fibers were wrapped around the fiber surface tightly and uniformly (Figs. 2e and S8), implying the conformal and uniform growth via ALD, as verified by the cross-sectional SEM image in Fig. 2f. In addition, the top surface of the AZO layer (the pink part in Fig. 2f) exhibited many small bulges resembling those of the pristine polyester fiber, which further demonstrated the superior conformability of ALD. Furthermore, the energy-dispersive X-ray spectroscopy (EDS) mapping images reveal the uniform distributions of four elements (C, O, Al and Zn) on single fiber (Fig. 2g), suggesting the adhesion of AZO films on the fiber surface (Fig. 2h and S9). Figure 2i shows the wide-scanning X-ray photoelectron spectroscopy (XPS) of CPF. It is evident that the CPF exhibits four peaks with binding energies at 1022.7, 532.0, 285.6 and 75.1 eV, assigning to Zn 2*p*, O 1*s*, C 1*s* and Al 2*p*, respectively. More narrowly, the CPF displays three carbon peaks, with binding energies at 284.6, 285.7 and 289.0 eV, which could be assigned to C–C, C–O–C and C=O bonding, respectively (Fig. S10a) [47]. The O 1*s* spectrum can be resolved into three peaks, with binding energies at 530.0, 531.5 and 532.4 eV, which is owing to O chemically bonded to the Zn, Al and physisorbed O at the surface, respectively (Fig. S10b) [65]. Moreover, the Al 2*p* spectrum showed one peak

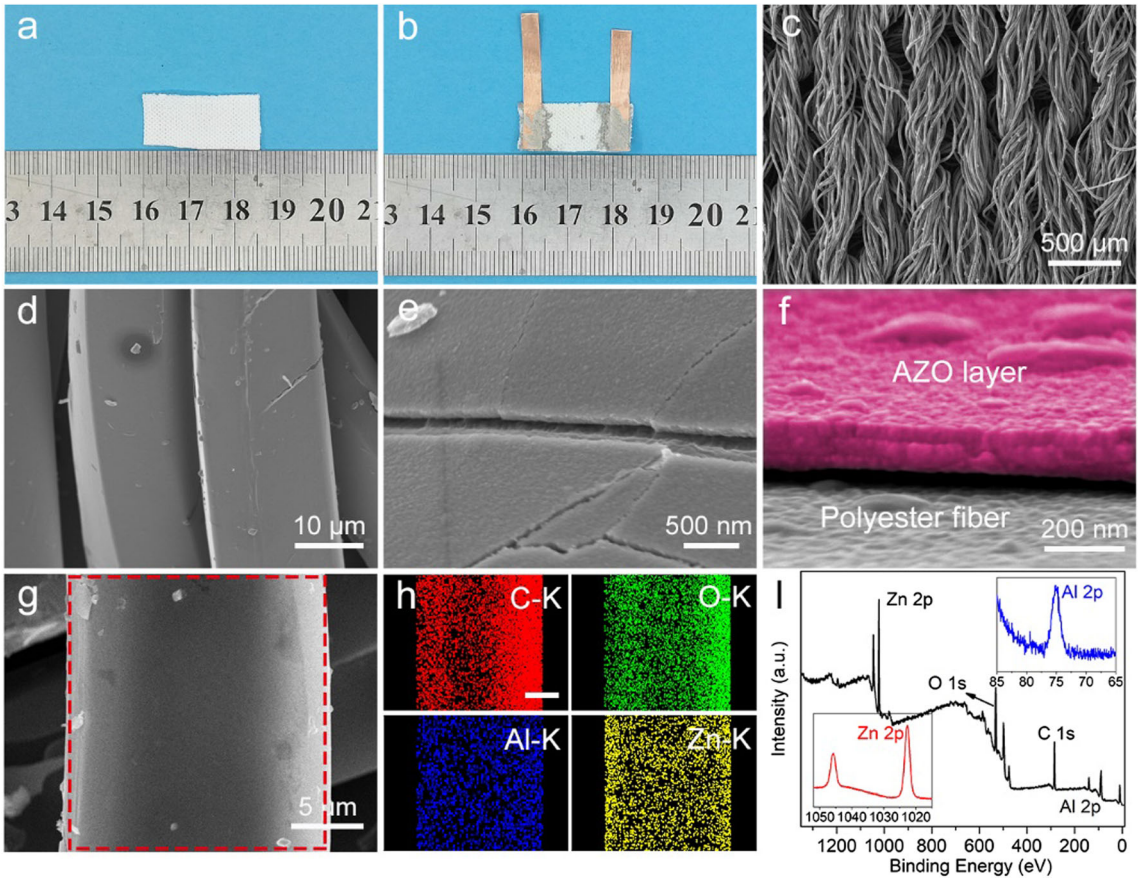

Figure 2 Morphologies and structures of the CPF strain sensor. Photographs of **a** a pristine polyester fabric and **b** the corresponding CPF strain sensor made from **a**. **c**, **d** SEM images of the conductive polyester fabric after AZO deposition with different magnifications. **e**, **f** SEM image and the cross-sectional SEM image of the AZO layer (the corresponding pink part) deposited on a single polyester fiber. **g**, **h** SEM image and the corresponding EDS mapping images: red, green, blue and yellow represent the C, O, Al and Zn element mapping results, respectively. **i** XPS spectrum of the conductive polyester fabric. The corresponding insets show the enlarged Al 2*p* and Zn 2*p* peaks, respectively.

centered at binding energy 74.0 eV represents Al^{3+} state of Al_2O_3 (Fig. S10c) [65]. Zn 2*p*3/2 and 2*p*1/2 peaks with binding energies at 1021.6 and 1044.7 eV, respectively, can be clearly observed in the Zn 2*p* spectrum of CPF (Fig. S10d) [66]. These results further verify the existence of AZO films on the polyester fabric.

Electromechanical performance of the CPF strain sensor

The CPF strain sensor showed excellent electromechanical performances. Figure 3a presents the tensile stress–strain curve of the CPF strain sensor. It can be seen that the CPF strain sensor exhibits high stretchability with large workable strain range of up to 130% owing to its weft-knitted structure. Besides, the tensile stress–strain curve of the fabric before ALD is displayed in Figure S11, which is consistent with the curve in Fig. 3a, implying the mechanical property of the fabric was not affected in the ALD and curing process. Figure 3b shows a typical plot of relative resistance change ($\Delta R/R_0$, $\Delta R = R - R_0$) versus the applied strain for the CPF strain sensor, where R_0 and R represent the initial and real-time resistances when being stretched, respectively. Interestingly, the CPF strain sensor exhibits a distinctive negative resistance variation with the strain range varying from 0 to 130% in contrast to the vast majority of reported textile strain sensor. The detailed mechanism will be discussed below. Generally, the gauge factor (GF), which is given by GF = $(\Delta R/R_0)/\varepsilon$ from the slope of the relative resistance change against the applied strain, is defined to evaluate the

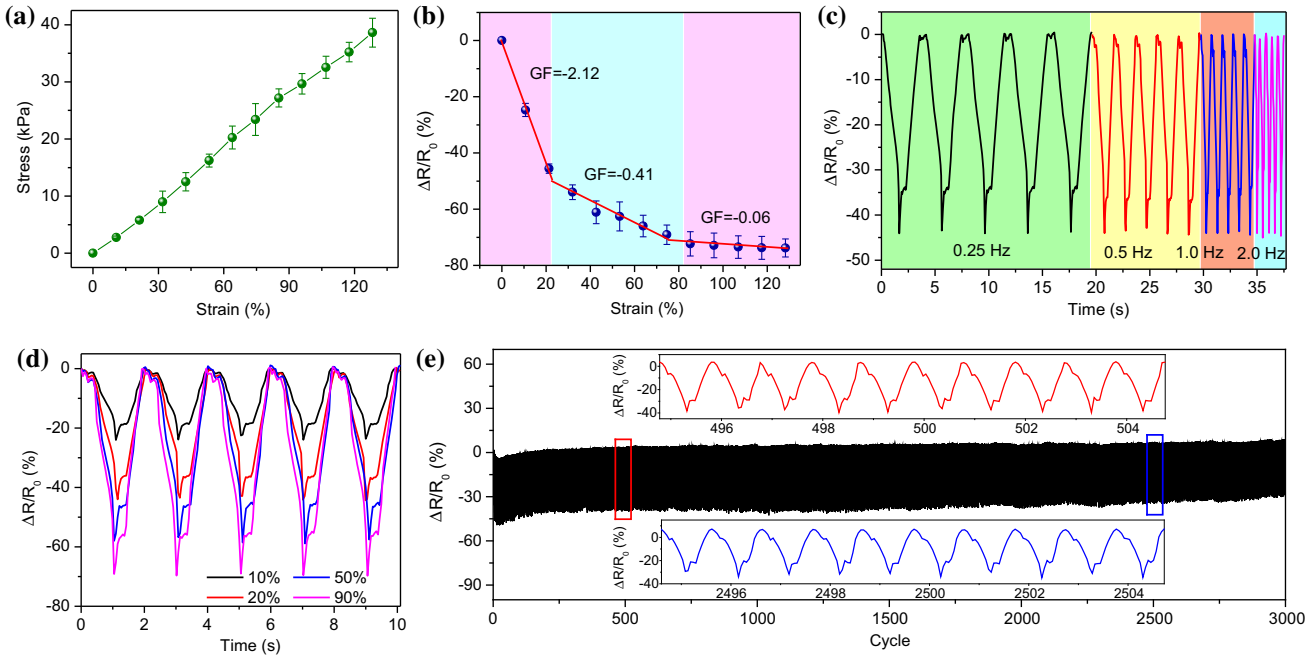

Figure 3 Electromechanical performances of the CPF strain sensor. **a** Tensile stress–strain curve of the CPF strain sensor. **b** Relative resistance change versus the applied strain. The strain rate is set to be 10 mm min^{-1}. **c** Relative resistance variation under cyclic stretching–releasing with a strain of 20% at frequency of 0.25, 0.5, 1.0 and 2.0 Hz. **d** Relative resistance change under various cyclic stretching–releasing strains at a frequency of 0.5 Hz. **e** Performance of the CPF strain sensor under 3000 stretching–releasing cycles of strain variation from 0 to 20% at a frequency of 1 Hz, with insets of the magnified cycles from the marked boxes.

sensitivity of the strain sensor. The curve presented in Fig. 3b could be divided into three linear regions, 0–20%, 20–80% and 80–130%, with a GF of − 2.12, − 0.41 and − 0.06, respectively, demonstrating both its sensitivity and wide workable strain range.

Figure 3c displays the relative resistance variation under cyclic stretching–releasing with a strain of 20% at frequency of 0.25, 0.5, 1.0 and 2.0 Hz, respectively. The $\Delta R/R_0$ of the CPF strain sensor was almost independent of the frequency within the tested frequency range (0.25–2.0 Hz), implying the excellent stability of the sensor under different frequencies. Furthermore, as shown in Fig. 3d, the relative resistance change of the CPF strain sensor showed reproducible and precise signals in response to different strains, manifesting superb electromechanical property of the CPF strain sensor in terms of the stability and repeatability. The intensity of signals increased proportionally as the strain increased, which was consistent with the results displayed in Fig. 3b. The response of the CPF strain sensor under a cyclic loading of 20% at a frequency of 1 Hz is presented in Fig. 3e. It is clear that the signals showed long-time stability for 3000 cycles, indicating its remarkable durability for numerous applications in our daily life. It should be mentioned that the output signals displayed a slight drift in this process, which can be attributed to the crack formation in AZO layers (Fig. S12).

Mechanical stability of the CPF strain sensor

It is well known that excellent mechanical stability is crucial for various practical applications of textile strain sensors. As proof-of-concept experiments, a series of tests were conducted to evaluate them. As shown in Fig. 4a and b, the friction test using a crockmeter with a loading pressure of 50 kPa was used to measure the rubbing resistance of the CPF according to the ISO 105 × 12 standard test method [67]. Both ends of the CPF were first fixed to the cotton using cellotape, and the CPF was subjected to reciprocating rubbing for 30 times. Apparently, the relative resistance change of the CPF under 20% strain after the rubbing test was exactly similar to that of CPF before the test, indicating its high rubbing resistance because of the formation of strong

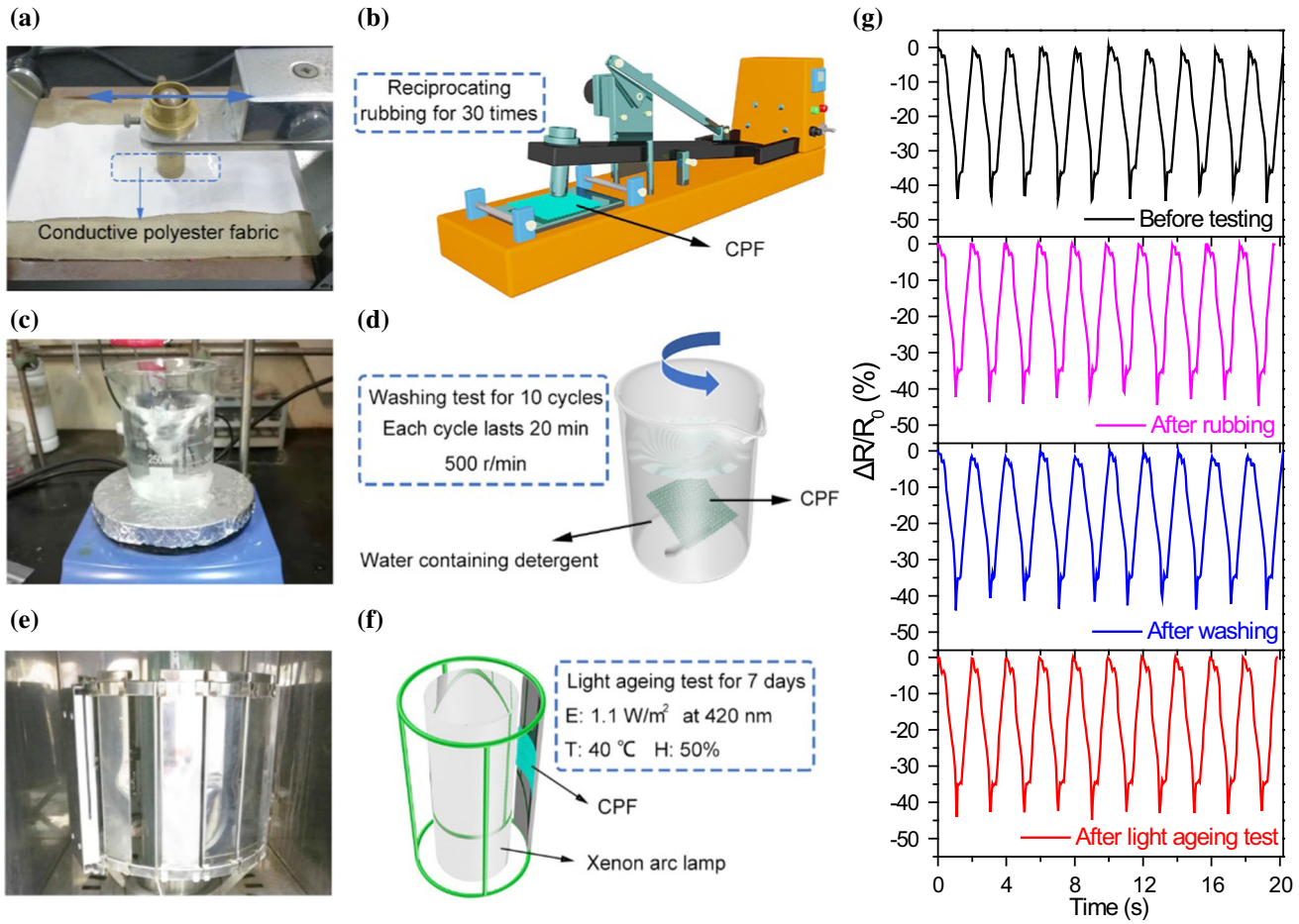

Figure 4 Mechanical stability of the CPF strain sensor. Digital photographs of the equipment for **a** the friction process simulation, **c** the washing process simulation and **e** the reactor chamber of a commercialized Sunlight Climate Tester, respectively. Schematic diagrams of **b** crockmeter, **d** washing model and **f** light aging test model, respectively. **g** Relative resistance changes of the CPF strain sensor under 20% strain at a frequency of 0.5 Hz before and after rubbing, washing and light aging test, respectively.

chemical interactions between AZO film and polyester fabric during ALD process (Fig. 4g). As a second mechanical stability test of CPF, its laundering durability was evaluated simulating the washing process environment, in which the CPF was placed in a beaker containing 200 mL of water under magnetically stirring at 500 r/min for 10 cycles (Fig. 4c, d). During the test, 0.2 mL of commercial laundry detergent was added and each washing cycle was set to 20 min. Figure 4g shows that no apparent difference was found between the two curves (black and blue curves) of relative resistance changes before and after washing test, implying its excellent laundering durability. This is rational because the strong adhesion of the AZO films to the polyester fibers originating from the chemical interactions as aforementioned. In addition to the rubbing resistance and laundering durability, light fastness is another factor that should be considered for textiles [62]. As displayed in Fig. 4e, f, CPF sample was tested using a commercialized Sunlight Climate Tester according to the standard of ISO 105-B02. In order to simulate the natural environment, a xenon arc lamp of 1.1 W m^{-2} irradiance at 420 nm equipped with water (humidity 50%) and wind was utilized to test the CPF sample. Figure 4g shows that the relative resistance change of the CPF under 20% strain after measurement for 7 days remained the same as that of CPF before the test, demonstrating its high light fastness. More importantly, the resistance values of CPF before and after rubbing, washing and light irradiation were measured, respectively, as shown in Figure S13 and Table S1 in Supporting Information. Although the resistance values were increased slightly after

rubbing and washing, the corresponding relative resistance changes were well maintained as confirmed by the above tests. Therefore, the above results demonstrated that the CPF fabricated by ALD technique possess excellent rubbing resistance, laundering durability and light fastness, which can offer great potential for numerous wearable applications.

Working mechanism of the CPF strain sensor

In order to understand the underlying mechanism of the relationship between relative resistance variation and stretchability, the morphology and structure evolution (Fig. 5a) under different strains are investigated. It can be clearly seen that a loop yarn consists of many twisted fibers, and the weft-knitted structure contains many repetitive loop structures in both horizontal and vertical directions (Fig. 5b). Apparently, a basic repetitive unit is composed of a complete loop yarn and two adjacent loop yarns which are directly contacted each other in parallel connection. Upon stretching, adjacent loop yarns perpendicular to tensile stress become more and more compact with the increase in strain, and the twisted fibers in the same loop yarn become closer accordingly, which are corresponding to the red dotted boxes in Fig. 5a. Based on that, we presumed simple resistance models to study the response mechanism. As shown in Fig. 5c, the original state resistance model corresponding to a basic repetitive unit can be regarded as a shunt circuit (Fig. 5d), in which the current flows through R_1–R_c–R_2–R_c and R_c–R_2–R_c–R_1 two paths separately. Therefore, the total original resistance R could be calculated by Eq. (1)

$$R = \frac{R_1 + R_2 + 2R_c}{2} \tag{1}$$

where R_1 and R_2 refer to the resistances in horizontal and vertical parts of one loop yarn, respectively. R_c denotes the contact resistance between two adjacent loop yarns in vertical direction without any applied strain. Initially there are some small gaps at the contact area between two adjacent loop yarns, thus contributing to a relatively large contact resistance inevitably. At this very moment, contact resistance is a critical factor to determine the total resistance. Compared to the contact resistance R_c, the resistances R_1 and R_2 are so small that can be ignored. Consequently, Eq. (1) can be simplified as $R = R_c$.

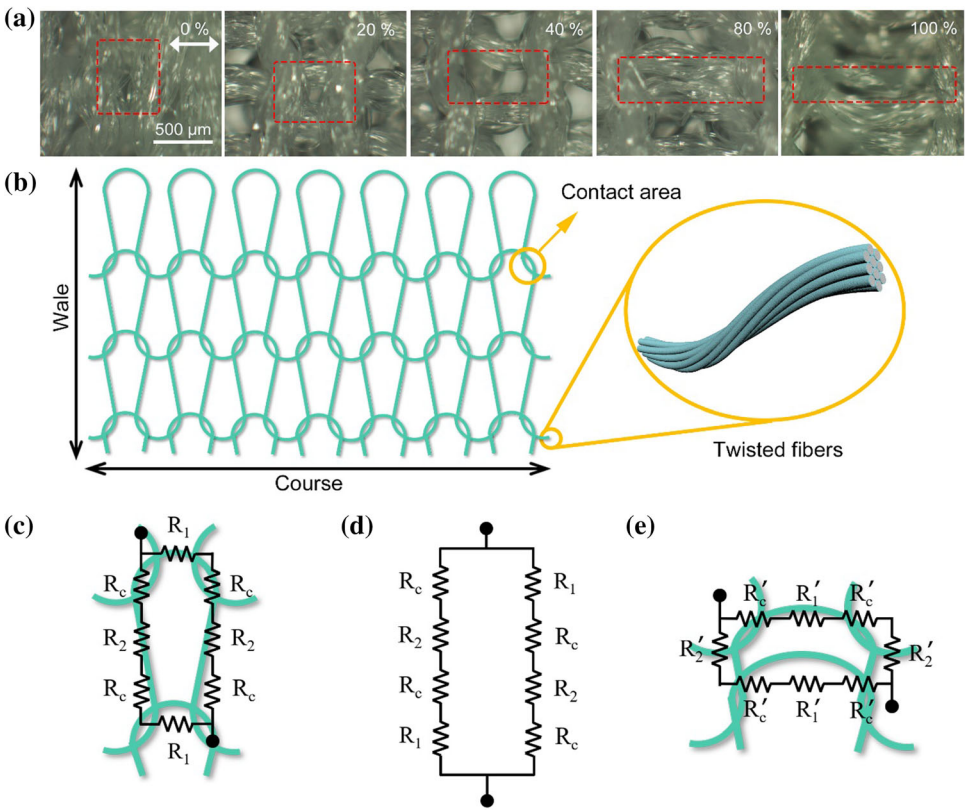

Figure 5 Working mechanism of the CPF strain sensor. **a** Optical images of the CPF strain sensor morphology at different strains. **b** Schematic illustration of the weft-knitted structure. **c** Original state resistance model of an elementary unit as shown in the red dotted box in **a** indicating the sensor without any loading. **d** Corresponding equivalent circuit diagram of the original state. **e** Resistance model of the sensor with stretching.

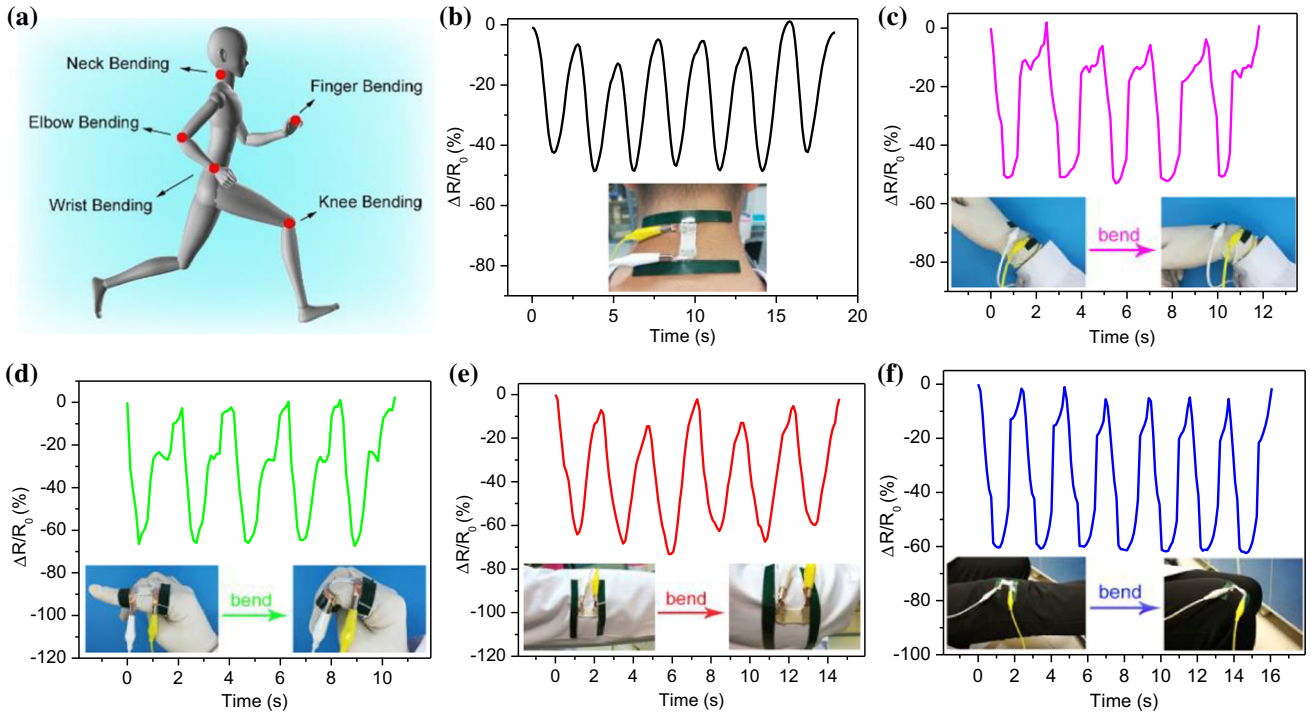

Figure 6 Detection of various human joint movements using the CPF strain sensors. **a** Schematic illustration of the sensor attached to different parts for detecting human joint movements. Corresponding time-dependent signals of **b** neck bending, **c** wrist bending, **d** finger bending, **e** elbow bending and **f** knee bending. The insets present photographs of the sensor fixed onto the relevant human joints.

During stretching, the contact areas at the junction will increase accordingly with increasing strain, thus leading to the reduction in the contact resistance (Fig. S14). This is the dominant factor for the decrease in the total resistance while stretching. Besides, the fibers in the same loop yarn become closer each other when stretching, which decreases the resistance of the yarn itself. Similarly, the current of the stretching state flows through R_c'–R_1'–R_c'–R_2' and R_2'–R_c'–R_1'–R_c' two paths separately (Fig. 5e). As a result, the total resistance R' with stretching could be described by Eq. (2)

$$R' = \frac{R_1' + R_2' + 2R_c'}{2} \tag{2}$$

where R_1', R_2' and R_c' are the resistances in horizontal and vertical parts of one loop yarn and the contact resistance between two adjacent loop yarns in vertical direction during the stretching process. According to the previous analysis, the resistances R_1', R_2' and R_c' are less than the corresponding resistances R_1, R_2 and R_c; thus, the stretching resistance R' is less than the original resistance R, which indicates the negative resistance variation of the sensor. To sum up, the above resistance model and analysis explicitly interpret the relationship between stretchability and relative resistance change.

Detection of the full-range human body movements

Owing to its high stretchability, breathability, excellent mechanical robustness and laundering durability, the CPF strain sensor could be directly knitted or sewed on garments or attached on human skin to detect the full-range human body movements. Figure 6a shows the schematic illustration of the sensor attached to different parts for monitoring diverse human joints movements. In Fig. 6a, the sensor was mounted on different human joints, such as the finger, wrist, knee, elbow and neck, to detect large human motions. For demonstration, a CPF strain sensor was attached to the neck (Fig. 6b) to monitor the motion of the neck joint. As shown in Fig. 6b, when the tester began to look down, the relative resistance change decreased immediately and reached a minimum value. With the recovery of the neck, the relative resistance change increased and

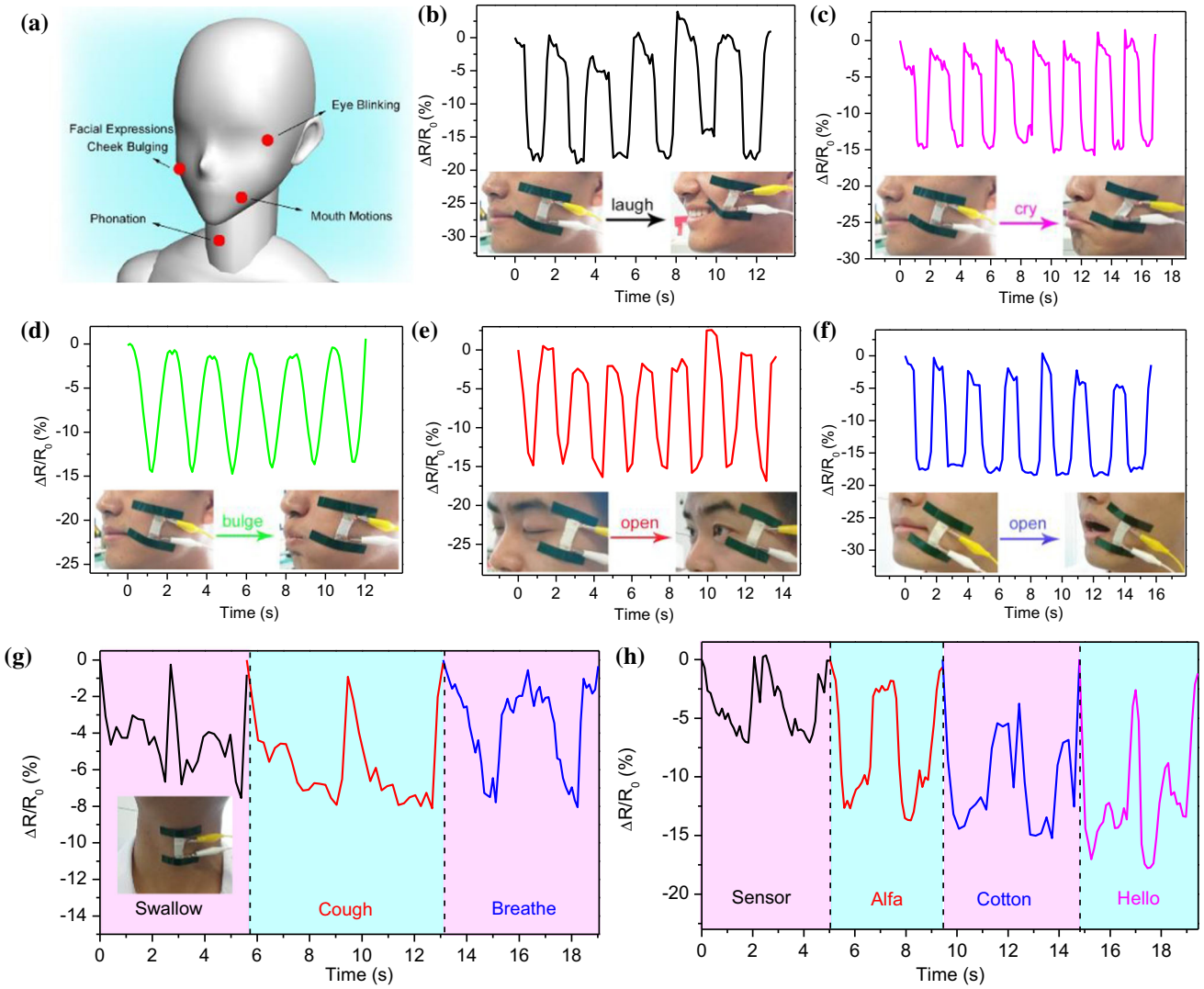

Figure 7 Applications of the CPF strain sensors for detecting various subtle human movements. **a** Schematic illustration of the sensor attached to different parts for detecting various subtle human movements. Corresponding time-dependent signals of facial expressions: **b** laughing and **c** crying. Signals showing the tiny muscle movements caused by **d** cheek bulging, **e** eye blinking and **f** mouth motions. **g** Corresponding signals when the tester was swallowing, coughing and breathing, respectively. **h** Signals of phonation when the tester pronounced different words.

returned to the original position, indicating its rapid and stable response to the cyclic motion of the neck during the monitoring process. Figure 6c shows a typical motion sensing of wrist. It is observed clearly that the relative resistance change declined promptly without apparent change when the wrist bended repeatedly. Similarly, several measurements are taken with continuous bending and stretching to detect the motions of finger, elbow and knee joints as evidenced in Fig. 6d–f, respectively, and the sensor also exhibited excellent performance. Therefore, the CPF strain sensor can be readily sewed on garments or attached on human skin for monitoring human motions, and the prompt and reversible response of the CPF strain sensor to the cyclic motion of joints shows great potential, with regard to its applications in large deformation of human body.

On the other hand, the CPF strain sensor can detect diverse subtle human motions promptly and accurately, such as tiny muscle movements, respiration, phonation and facial expressions. We attached the sensor to different parts for detecting various subtle human movements, as schematically shown in Fig. 7a. As demonstrated, facial expressions of

laughing and crying could be detected and recognized by fixing the sensor onto the cheek, and the corresponding signals are demonstrated in Fig. 7b, c, respectively. Obviously, the relative resistance change induced by tiny movements of the facial muscles could be precisely recorded. Besides, when the tester repeated cheek bulging, the signal showed quite good repetitive patterns, which demonstrated its excellent reliability and stability of the sensor (Fig. 7d). In Fig. 7e, the relative resistance change induced by blinking could also be tracked and perceived accurately when the CPF strain sensor was attached to the corner of an eye (inset in Fig. 7e). Figure 7f presents the relative resistance change when mouth is open and closed. Furthermore, the changes in muscle movements can be recognized by mounting the sensor onto the throat, when the tester swallowed water, coughed slightly and breathed, the distinct characteristic signals (intensity and shape) of curves differentiate these tiny muscle vibrations from each other as shown in Fig. 7g. More interestingly, the CPF strain sensor also can be used to distinguish the motion of throat induced by pronouncing different words. Figure 7h shows the performance of the sensor in phonation. It can be seen that the sensor displayed distinguishable and repeatable signal patterns for each word, which endowed the sensor potential applications in phonation rehabilitation training and human–machine interaction. Therefore, the above results demonstrate the excellent performance of the CPF strain sensor in detecting subtle deformations of the human body.

Conclusion

In summary, we have developed a highly stretchable, breathable textile strain sensor with excellent mechanical robustness and laundering durability based on polyester fabric via ALD and demonstrated its superior performance in detecting both large and subtle movements. The CPF strain sensor derived from weft-knitted structure exhibits high stretchability up to 130%, sensitivity (GF of − 2.12 under 0–20%, GF of − 0.41 under 20–80% and that of − 0.06 under 80–130%) and a distinct negative resistance variation with increasing strain. More importantly, owing to the formation of the chemical interactions between AZO film and textile, the CPF strain sensor possesses excellent mechanical robustness, laundering durability and long-term stability (3000 cycles), which are critical factors for truly practical uses of wearable devices. Notably, the CPF strain sensor can be used directly for practical applications without the elastic polymer encapsulation, which endows the sensor with excellent breathability and great comfort. Based on that, we demonstrate that the CPF strain sensor can be used in detection of both large deformations (joint movement) and subtle movements (facial expressions, phonation, etc.) of the human body, indicating its tremendous potential applications in wearable electronics. It can be predicted that this approach for fabricating textile strain sensor can be readily extended to other fabrics such as cotton, wool, silk and especially various colored textiles, paving a new way for the fabrication of wearable textile sensor with excellent mechanical stability and breathability.

Acknowledgements

The work was supported by the Key Program of National Natural Science Foundation of China (21536002), the National Natural Science Foundation of China (21506023), Natural Science Foundation of Liaoning Province (20180550501), the Fundamental Research Funds for the Central Universities (DUT19JC14), the Fund for innovative research groups of the National Natural Science Fund Committee of Science (21421005) and the Innovation Research Team in University (IRT_13R06).

Compliance with ethical standards

Conflict of interest The authors declare no competing financial interest.

Electronic supplementary material: The online version of this article (https://doi.org/10.1007/s10853-019-04189-x) contains supplementary material, which is available to authorized users.

References

[1] Amjadi M, Kyung KU, Park I, Sitti M (2016) Stretchable, skin-mountable, and wearable strain sensors and their potential applications: a review. Adv Funct Mater 26:1678–1698

[2] Liu Y, Pharr M, Salvatore GA (2017) Lab-on-skin: a review of flexible and stretchable electronics for wearable health monitoring. ACS Nano 11:9614–9635

[3] Rogers JA, Someya T, Huang YG (2010) Materials and mechanics for stretchable electronics. Science 327:1603–1607

[4] Trung TQ, Lee NE (2016) Flexible and stretchable physical sensor integrated platforms for wearable human-activity monitoring and personal healthcare. Adv Mater 28:4338–4372

[5] Wang CY, Xia KL, Wang HM, Liang XP, Yin Z, Zhang YY (2019) Advanced carbon for flexible and wearable electronics. Adv Mater 31:1801072

[6] Du DH, Li PC, Ouyang JY (2016) Graphene coated nonwoven fabrics as wearable sensors. J Mater Chem C 4:3224–3230

[7] Ma JH, Wang P, Chen HY, Bao SJ, Chen W, Lu HB (2019) Highly sensitive and large-range strain sensor with a self-compensated two-order structure for human motion detection. ACS Appl Mater Interfaces 11:8527–8536

[8] Yamada T, Hayamizu Y, Yamamoto Y, Yomogida Y, Izadi-Najafabadi A, Futaba DN, Hata K (2011) A stretchable carbon nanotube strain sensor for human-motion detection. Nat Nanotechnol 6:296–301

[9] Yao SS, Zhu Y (2014) Wearable multifunctional sensors using printed stretchable conductors made of silver nanowires. Nanoscale 6:2345–2352

[10] Yin B, Wen YW, Hong T, Xie ZS, Yuan GL, Ji QM, Jia HB (2017) Highly stretchable, ultrasensitive, and wearable strain sensors based on facilely prepared reduced graphene oxide woven fabrics in an ethanol flame. ACS Appl Mater Interfaces 9:32054–32064

[11] Zhang HX, Niu WB, Zhang SF (2018) Extremely stretchable, stable, and durable strain sensors based on double-network organogels. ACS Appl Mater Interfaces 10:32640–32648

[12] Li LH, Bai YY, Li LL, Wang SQ, Zhang T (2017) A superhydrophobic smart coating for flexible and wearable sensing electronics. Adv Mater 29:1702517

[13] Liu YQ, He K, Chen G, Leow WR, Chen XD (2017) Nature-inspired structural materials for flexible electronic devices. Chem Rev 117:12893–12941

[14] Yang TT, Wang W, Zhang HZ, Li XM, Shi JD, He YJ, Zheng QS, Li ZH, Zhu HW (2015) Tactile sensing system based on arrays of graphene woven microfabrics: electromechanical behavior and electronic skin application. ACS Nano 9:10867–10875

[15] Bauer S, Bauer-Gogonea S, Graz I, Kaltenbrunner M, Keplinger C, Schwodiauer R (2014) 25th anniversary article: a soft future: from robots and sensor skin to energy harvesters. Adv Mater 26:149–162

[16] Wang CY, Li X, Gao EL, Jian MQ, Xia KL, Wang Q, Xu ZP, Ren TL, Zhang YY (2016) Carbonized silk fabric for ultrastretchable, highly sensitive, and wearable strain sensors. Adv Mater 28:6640–6648

[17] Wang Y, Wang L, Yang TT, Li X, Zang XB, Zhu M, Wang KL, Wu DH, Zhu HW (2014) Wearable and highly sensitive graphene strain sensors for human motion monitoring. Adv Funct Mater 24:4666–4670

[18] Liu X, Tang C, Du XH, Xiong SA, Xi SY, Liu YF, Shen X, Zheng QB, Wang ZY, Wu Y, Horner A, Kim JK (2017) A highly sensitive graphene woven fabric strain sensor for wearable wireless musical instruments. Mater Horiz 4:477–486

[19] Roh E, Hwang BU, Kim D, Kim BY, Lee NE (2015) Stretchable, transparent, ultrasensitive, and patchable strain sensor for human–machine interfaces comprising a nanohybrid of carbon nanotubes and conductive elastomers. ACS Nano 9:6252–6261

[20] Boland CS, Khan U, Backes C, O'Neill A, McCauley J, Duane S, Shanker R, Liu Y, Jurewicz I, Dalton AB, Coleman JN (2014) Sensitive, high-strain, high-rate bodily motion sensors based on graphene–rubber composites. ACS Nano 8:8819–8830

[21] Christ JF, Aliheidari N, Ameli A, Pötschke P (2017) 3D printed highly elastic strain sensors of multiwalled carbon nanotube/thermoplastic polyurethane nanocomposites. Mater Des 131:394–401

[22] Liu H, Gao JC, Huang WJ, Dai K, Zheng GQ, Liu CT, Shen CY, Yan XR, Guo J, Guo ZH (2016) Electrically conductive strain sensing polyurethane nanocomposites with synergistic carbon nanotubes and graphene bifillers. Nanoscale 8:12977–12989

[23] Shi G, Zhao ZH, Pai JH, Lee I, Zhang LQ, Stevenson C, Ishara K, Zhang RJ, Zhu HW, Ma J (2016) Highly sensitive, wearable, durable strain sensors and stretchable conductors using graphene/silicon rubber composites. Adv Funct Mater 26:7614–7625

[24] Liu ZY, Qi DP, Guo PZ, Liu Y, Zhu BW, Yang H, Liu YQ, Li B, Zhang CG, Yu JC, Liedberg B, Chen XD (2015) Thickness-gradient films for high gauge factor stretchable strain sensors. Adv Mater 27:6230–6237

[25] Yan CY, Wang JX, Kang WB, Cui MQ, Wang X, Foo CY, Chee KJ, Lee PS (2014) Highly stretchable piezoresistive graphene–nanocellulose nanopaper for strain sensors. Adv Mater 26:2022–2027

[26] Zhang C, Li H, Huang A, Zhang Q, Rui K, Lin H, Sun G, Zhu J, Peng H, Huang W (2019) Rational design of a flexible

CNTs@PDMS film patterned by bio-inspired templates as a strain sensor and supercapacitor. Small 15:e1805493

[27] Zhang MC, Wang CY, Wang HM, Jian MQ, Hao XY, Zhang YY (2017) Carbonized cotton fabric for high-performance wearable strain sensors. Adv Funct Mater 27:1604795

[28] Kim SJ, Song W, Yi Y, Min BK, Mondal S, An KS, Choi CG (2018) High durability and waterproofing rGO/SWCNT-fabric-based multifunctional sensors for human-motion detection. ACS Appl Mater Interfaces 10:3921–3928

[29] Seyedin S, Zhang P, Naebe M, Qin S, Chen J, Wang XA, Razal JM (2019) Textile strain sensors: a review of the fabrication technologies, performance evaluation and applications. Mater Horiz 6:219–249

[30] Souri H, Bhattacharyya D (2018) Highly stretchable multifunctional wearable devices based on conductive cotton and wool fabrics. ACS Appl Mater Interfaces 10:20845–20853

[31] Yang Z, Pang Y, Han XL, Yang YF, Ling J, Jian MQ, Zhang YY, Yang Y, Ren TL (2018) Graphene textile strain sensor with negative resistance variation for human motion detection. ACS Nano 12:9134–9141

[32] Cataldi P, Dussoni S, Ceseracciu L, Maggiali M, Natale L, Metta G, Athanassiou A, Bayer IS (2018) Carbon nanofiber versus graphene-based stretchable capacitive touch sensors for artificial electronic skin. Adv Sci 5:1700587

[33] Li MF, Li HY, Zhong WB, Zhao QH, Wang D (2014) Stretchable conductive polypyrrole/polyurethane (PPy/PU) strain sensor with netlike microcracks for human breath detection. ACS Appl Mater Interfaces 6:1313–1319

[34] Wang X, Sparkman J, Gou J (2017) Strain sensing of printed carbon nanotube sensors on polyurethane substrate with spray deposition modeling. Compos Commun 3:1–6

[35] Trung TQ, Dang TML, Ramasundaram S, Toi PT, Park SY, Lee NE (2019) A stretchable strain-insensitive temperature sensor based on free-standing elastomeric composite fibers for on-body monitoring of skin temperature. ACS Appl Mater Interfaces 11:2317–2327

[36] Cai GM, Yang MY, Xu ZL, Liu JG, Tang B, Wang XG (2017) Flexible and wearable strain sensing fabrics. Chem Eng J 325:396–403

[37] Lee T, Lee W, Kim SW, Kim JJ, Kim BS (2016) Flexible textile strain wireless sensor functionalized with hybrid carbon nanomaterials supported ZnO nanowires with controlled aspect ratio. Adv Funct Mater 26:6206–6214

[38] Li YD, Li YN, Su M, Li WB, Li YF, Li HZ, Qian X, Zhang XY, Li FY, Song YL (2017) Electronic textile by dyeing method for multiresolution physical kineses monitoring. Adv Electron Mater 3:1700253

[39] Ren JS, Wang CX, Zhang X, Carey T, Chen KL, Yin YJ, Torrisi F (2017) Environmentally-friendly conductive cotton fabric as flexible strain sensor based on hot press reduced graphene oxide. Carbon 111:622–630

[40] Robert C, Feller JF, Castro M (2012) Sensing skin for strain monitoring made of PC-CNT conductive polymer nanocomposite sprayed layer by layer. ACS Appl Mater Interfaces 4:3508–3516

[41] Amjadi M, Pichitpajongkit A, Lee S, Ryu S, Park I (2014) Highly stretchable and sensitive strain sensor based on silver nanowire-elastomer nanocomposite. ACS Nano 8:5154–5163

[42] Yang Z, Wang DY, Pang Y, Li YX, Wang Q, Zhang TY, Wang JB, Liu X, Yang YY, Jian JM, Jian MQ, Zhang YY, Yang Y, Ren TL (2018) Simultaneously detecting subtle and intensive human motions based on a silver nanoparticles bridged graphene strain sensor. ACS Appl Mater Interfaces 10:3948–3954

[43] Zhang MC, Wang CY, Wang Q, Jian MQ, Zhang YY (2016) Sheath-core graphite/silk fiber made by dry-meyer-rod-coating for wearable strain sensors. ACS Appl Mater Interfaces 8:20894–20899

[44] Cataldi P, Ceseracciu L, Athanassiou A, Bayer IS (2017) Healable cotton–graphene nanocomposite conductor for wearable electronics. ACS Appl Mater Interfaces 9:13825–13830

[45] Huang GW, Xiao HM, Fu SY (2015) Wearable electronics of silver-nanowire/poly(dimethylsiloxane) nanocomposite for smart clothing. Sci Rep 5:13971

[46] Cao YQ, Cao ZY, Li X, Wu D, Li AD (2014) A facile way to deposit conformal Al_2O_3 thin film on pristine graphene by atomic layer deposition. Appl Surf Sci 291:78–82

[47] Chen FX, Yang HY, Li K, Deng B, Li QS, Liu X, Dong BH, Xiao XF, Wang D, Qin Y, Wang SM, Zhang KQ, Xu WL (2017) Facile and effective coloration of dye-inert carbon fiber fabrics with tunable colors and excellent laundering durability. ACS Nano 11:10330–10336

[48] Detavernier C, Dendooven J, Sree SP, Ludwig KF, Martens JA (2011) Tailoring nanoporous materials by atomic layer deposition. Chem Soc Rev 40:5242–5253

[49] George SM (2010) Atomic layer deposition: an overview. Chem Rev 110:111–131

[50] Chen XY, Zhu HL, Chen YC, Shang YY, Cao AY, Hu LB, Rubloff GW (2012) MWCNT/V_2O_5 core/shell sponge for high areal capacity and power density Li-ion cathodes. ACS Nano 6:7948–7955

[51] Gui Z, Zhu HL, Gillette E, Han XG, Rubloff GW, Hu LB, Lee SB (2013) Natural cellulose fiber as substrate for supercapacitor. ACS Nano 7:6037–6046

[52] Jur JS, Spagnola JC, Lee K, Gong B, Peng Q, Parsons GN (2010) Temperature-dependent subsurface growth during

atomic layer deposition on polypropylene and cellulose fibers. Langmuir 26:8239–8244

[53] Lee J, Yoon J, Kim HG, Kang S, Oh WS, Algadi H, Al-Sayari S, Shong B, Kim SH, Kim H, Lee T, Lee HBR (2016) Highly conductive and flexible fiber for textile electronics obtained by extremely low-temperature atomic layer deposition of Pt. NPG Asia Mater 8:e331

[54] Vogel NA, Williams PS, Brozena AH, Sen D, Atanasov S, Parsons GN, Khan SA (2015) Delayed dissolution and small molecule release from atomic layer deposition coated electrospun nanofibers. Adv Mater Interfaces 2:1500229

[55] Dasgupta NP, Neubert S, Lee W, Trejo O, Lee JR, Prinz FB (2010) Atomic layer deposition of Al-doped ZnO films: effect of grain orientation on conductivity. Chem Mater 22:4769–4775

[56] Kwon JH, Jeon Y, Choi KC (2018) Robust transparent and conductive gas diffusion multibarrier based on Mg- and Al-doped ZnO as indium tin oxide-free electrodes for organic electronics. ACS Appl Mater Interfaces 10:32387–32396

[57] Na JS, Peng Q, Scarel G, Parsons GN (2009) Role of gas doping sequence in surface reactions and dopant incorporation during atomic layer deposition of Al-doped ZnO. Chem Mater 21:5585–5593

[58] Zhai CH, Zhang RJ, Chen X, Zheng YX, Wang SY, Liu J, Dai N, Chen LY (2016) Effects of Al doping on the properties of ZnO thin films deposited by atomic layer deposition. Nanoscale Res Lett 11:407

[59] Biccai S, Boland CS, O'Driscoll DP, Harvey A, Gabbett C, O'Suilleabhain DR, Griffin AJ, Li ZL, Young RJ, Coleman JN (2019) Negative gauge factor piezoresistive composites based on polymers filled with MoS_2 nanosheets. ACS Nano 13:6845–6855

[60] Zhang MC, Wang CY, Liang XP, Yin Z, Xia KL, Wang H, Jian MQ, Zhang YY (2017) Weft-knitted fabric for a highly stretchable and low-voltage wearable heater. Adv Electron Mater 3:1700193

[61] Elliott SD, Dey G, Maimaiti Y, Ablat H, Filatova EA, Fomengia GN (2016) Modeling mechanism and growth reactions for new nanofabrication processes by atomic layer deposition. Adv Mater 28:5367–5380

[62] Niu W, Zhang L, Wang Y, Zhang S (2019) Multicolored one-dimensional photonic crystal coatings with excellent mechanical robustness, strong substrate adhesion, and liquid and particle impalement resistance. J Mater Chem C 7:3463–3470

[63] Lee SM, Pippel E, Gosele U, Dresbach C, Qin Y, Chandran CV, Brauniger T, Hause G, Knez M (2009) Greatly increased toughness of infiltrated spider silk. Science 324:488–492

[64] Vervuurt RHJ, Karasulu B, Verheijen MA, Kessels WMM, Bol AA (2017) Uniform atomic layer deposition of Al_2O_3 on graphene by reversible hydrogen plasma functionalization. Chem Mater 29:2090–2100

[65] Wen L, Sahu BB, Kim HR, Han JG (2019) Study on the electrical, optical, structural, and morphological properties of highly transparent and conductive AZO thin films prepared near room temperature. Appl Surf Sci 473:649–656

[66] Hussain SQ, Le AHT, Mallem K, Park H, Ju M, Kim Y, Cho J, Park J, Kim Y, Yi J (2018) Using the light scattering properties of multi-textured AZO films on inverted hemisphere textured glass surface morphologies to improve the efficiency of silicon thin film solar cells. Appl Surf Sci 447:866–875

[67] Meng Y, Tang BT, Ju BZ, Wu SL, Zhang SF (2017) Multiple colors output on voile through 3D colloidal crystals with robust mechanical properties. ACS Appl Mater Interfaces 9:3024–3029